PHYSICAL REVIEW B **95**, 144411 (2017)

Counter-rotating standing spin waves: A magneto-optical illusion

S. Shihab,[1] L. Thevenard,[1] A. Lemaître,[2] and C. Gourdon[1,*]

[1]*Sorbonne Universités, UPMC Univ Paris 06, CNRS-UMR 7588, Institut des NanoSciences de Paris, F-75005, Paris, France*

[2]*Centre de Nanosciences et Nanotechnologies, CNRS, Univ. Paris-Sud, Université Paris-Saclay, 91460 Marcoussis, F-91460 France*

(Received 28 October 2016; revised manuscript received 22 March 2017; published 12 April 2017)

We excite perpendicular standing spin waves by a laser pulse in a GaMnAsP ferromagnetic layer and detect them using time-resolved magneto-optical effects. Quite counterintuitively, we find the first two excited modes to be of opposite chirality. We show that this can only be explained by taking into account absorption and optical phase shift inside the layer. This optical illusion is particularly strong in weakly absorbing layers. These results provide a correct identification of spin waves modes, enabling a trustworthy estimation of their respective weight as well as an unambiguous determination of the spin stiffness parameter.

DOI: 10.1103/PhysRevB.95.144411

I. INTRODUCTION

Since pioneering work on nickel [1], laser-induced magnetization dynamics has been widely used to investigate ultrafast magnetic processes not only in magnetic metals [2,3] but also in magnetic semiconductors [4–9] and insulators [10,11], exploring the fundamentals of light-spin interaction in view of a full and ultrafast optical control of magnetic order.

Ultrashort pulses can trigger a wide variety of processes, including ultrafast demagnetization [1], full magnetization reversal [12], as well as coherent precession [2,4,10]. In magnetically ordered materials, ferro- and ferrimagnets, as well as in antiferromagnets, the coherent magnetization dynamics arises from collective spin excitations, spin waves (SW) (or magnons, their quanta), which attract considerable interest motivated by their possible use as information carriers in magnonics applications [13,14]. Magnons are versatile excitations since their dispersion curves, comprising magnetostatic and exchange modes [15], can be tuned by a magnetic field or by micro- or nanostructuring the material in any of its dimensions [14]. For instance, perpendicular standing spin-wave (PSSW) modes in a single nanometric layer of thickness L with free boundary conditions (no surface anisotropy) will have their wave vector quantized by an integer p ($k = p\pi/L$), and their energy by p^2, proportionally to the spin stiffness D.

SWs can be studied in the frequency domain by, e.g., ferromagnetic resonance (FMR) experiments or Brillouin light scattering as well as in the time domain by time-resolved laser pump-probe experiments using magneto-optical effects. The latter distinguish themselves in various ways from the former. The *coherent* excitation of several PSSWs with different frequencies, from the sub-GHz to the THz range, is made possible by the wide frequency spectrum of the pulsed excitation induced by the femtosecond pump laser pulses. In a single time scan pump-probe experiments can detect several coherent SW modes and provide their time period, their respective phases, and their damping. Coherent control experiments using two pump beams can be performed [16,17]. Furthermore the possibility to fully reconstruct the magnetization trajectory using two different magneto-optical effects [18,19] brings a deep insight into magnetization dynamics.

Whereas the excitation mechanism of SWs by optical, acoustical, or magnetic field pulses [14,20–22], has been thoroughly discussed, their optical detection has been much less addressed [4,23]. In particular, in contrast to the cavity FMR detection of SWs which was modeled a long time ago [24], the respective amplitudes of optically detected SWs remained unexplained [2,9,14,25]. In this paper, we provide a comprehensive model to explain the large amplitude of these nonuniform SWs that should not be detectable in the framework of simple models [4]. We moreover present intriguing experimental results of apparent different chiralities for SWs of different parities. We show that they can only be explained by our theoretical description of the magneto-optical detection through the Kerr and Voigt effects that takes into account the absorption depth and the optical phase shift inside the layer. Important consequences are expected when the SW wavelength (determined by the layer thickness) becomes a few tenth of the wavelength of light in the material, λ/η, where η is the refractive index. In particular, ignoring this effect can lead to an erroneous determination of the SW stiffness, and of the relative mode amplitude, a signature of the up-to-now elusive magnon excitation mechanisms. We show that the optical phase shift can lead to a striking and nonintuitive optical effect in the detection of SWs: an apparent reversal of the magnetization rotation direction for SWs of odd parity with respect to the layer midplane. A key result of this paper is that the optical phase shift provides a unique tool for the determination of the SW mode number, or in other words its parity.

II. SAMPLES AND EXPERIMENTAL SETUP

We study thin layers of the ferromagnetic semiconductor alloy GaMnAsP. Most samples show only one PSSW mode in the FMR spectra while one or two modes are optically detected in the TRMO signal [8,26]. The results presented here are obtained in an in-plane magnetized GaMnAsP layer with thickness $L = 50$ nm and phosphorus concentration 4.3% grown on a (001) GaAs substrate by molecular beam epitaxy and annealed 1 hour at 250 °C. The effective Mn concentration is 4% and the Curie temperature is 85 K. The anisotropy constants were determined by FMR. Pump-probe experiments are carried out at $T = 12$ K in zero external magnetic field after a 60 mT in-plane initialization of the magnetization

---

[*] gourdon@insp.jussieu.fr

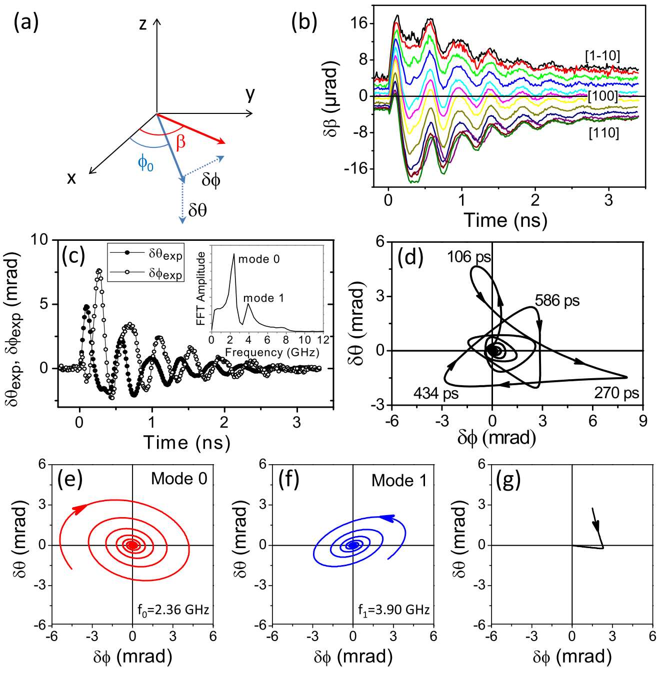

FIG. 1. (a) Reference frame. (b) Dependence of the TRMO signal $\delta\beta$ on the probe beam linear polarization with respect to the sample crystallographic axes. (c) Time dependence of $\delta\theta_{\text{exp}}$ and $\delta\phi_{\text{exp}}$. Inset: Fourier transform amplitude of $\delta\theta_{\text{exp}}$. (d) Optically detected magnetization trajectory. (e), (f), (g) Decomposition of the experimental magnetization trajectory (d) into two oscillating signals at frequencies $f_0 = 2.36$ GHz and $f_1 = 3.90$ GHz and a nonoscillating signal, respectively.

direction. The laser source is a 76 MHz Ti:Sapphire laser at a wavelength $\lambda = 700$ nm. To limit thermal effects, low pump and probe fluence are used ($1\,\mu J\,\text{cm}^{-2}$ and $0.4\,\mu J\,\text{cm}^{-2}$, respectively) [27]. The pump beam is modulated at 50 kHz. The pump-induced magnetization dynamics is detected as a function of the pump-probe delay through the rotation of the probe beam linear polarization detected by a balanced optical diode bridge and a lock-in amplifier. The static rotation and ellipticity signals are obtained with the probe beam only.

III. EXPERIMENTAL RESULTS

The existence of circular and linear magnetic birefringence/dichroism [28] makes the TRMO signal sensitive to both the out-of-plane $\delta\theta$ and the in-plane $\delta\phi$ components of the transient magnetization [Fig. 1(a)]. This allows for the reconstruction of the magnetization trajectory using the expected dependency of the rotation angle $\delta\beta_r$ on the probe polarization angle β (Ref. [19] and Appendix):

$$\delta\beta_r^{\text{exp}}(t) = K_r\delta\theta_{\text{exp}}(t) + 2V_r\delta\phi_{\text{exp}}(t)\cos 2(\beta-\phi_0)$$
$$-2V_r\frac{\delta M(t)}{M}\sin 2(\beta-\phi_0), \qquad (1)$$

where K_r and V_r are the static Kerr and Voigt rotation coefficients, M is the magnetization vector modulus, and ϕ_0 is the in-plane equilibrium angle of the magnetization.

Figure 1(b) shows the dependence of the TRMO signal on the incident probe polarization. The signal is fitted with $u(t) + v(t)\sin 2\beta + w(t)\cos 2\beta$ from which we obtain the $\delta\theta_{\text{exp}}(t)$ and $\delta\phi_{\text{exp}}(t)$ functions taking into account the magnetization equilibrium angle ϕ_0 (**M** close to [100]) as shown in Fig. 1(c) (see Appendix). The plot of the trajectory, $\delta\theta_{\text{exp}}(t)$ versus $\delta\phi_{\text{exp}}(t)$ shown in Fig. 1(d), reveals a very complex dynamics that actually results from the contributions of two SWs that clearly appear in $\delta\theta_{\text{exp}}(t)$ and $\delta\phi_{\text{exp}}(t)$ and their Fourier transform [Fig. 1(c) and inset]. Let us note the large ratio (≈ 0.6) of the amplitude of the second SW with respect to the first one. $\delta\theta_{\text{exp}}(t)$ and $\delta\phi_{\text{exp}}(t)$ are fitted with two damped oscillating signals and a sum of two exponentials that reflects the shape of the laser-induced pulsed excitation ($\tau_1 = 0.03$ ns, $\tau_2 = 1$ ns). Plotting separately the trajectory for each SW ($f_0 = 2.36$ GHz and $f_1 = 3.90$ GHz) in Figs. 1(e) and 1(f) results in a much clearer picture of the magnetization precession. Surprisingly, the magnetization seems to rotate in *opposite* directions for the two SWs. As we shall see below, this is an "optical illusion" resulting from an optical phase shift inside the layer. To demonstrate this, we first describe the SW excitation by a laser pulse using the Landau-Lifshitz-Gilbert (LLG) equation and appropriate boundary conditions at the top and bottom interfaces. We then calculate the detected magneto-optical signal using a multilayer and transfer matrix model, which we show to be indispensable to recover the observed SWs chiralities.

IV. MODEL

The SW space and time profiles are obtained by solving the LLG equation within the small precession angle approximation for in-plane static magnetization:

$$\dot{\delta\phi} = \gamma\left(F_{\theta\theta}\,\delta\theta - D\frac{\partial^2\delta\theta}{\partial z^2}\right) + \alpha_G\dot{\delta\theta}$$
$$\dot{\delta\theta} = -\gamma\left(F_{\phi\phi}\,\delta\phi - D\frac{\partial^2\delta\phi}{\partial z^2} + \delta B_{\text{exc}}(z,t)\right) - \alpha_G\,\dot{\delta\phi}. \qquad (2)$$

F is equal to E/M where E is the magnetic anisotropy energy [29]. α_G is the Gilbert damping. $F_{i,j} = \frac{\partial^2 F}{\partial i\partial j}$ are the second derivatives of F with respect to the angles (i,j). Since it was shown that in thin (Ga,Mn)(As,P) layers the lowest frequency PSSW is a nearly uniform mode, independent of the layer thickness [8,9], the boundary conditions at $z = 0$ and $z = L$ were chosen to ensure very weak surface pinning, giving nearly flat $\delta\theta(z)$ and $\delta\phi(z)$ profiles at any t for this mode (see Appendix Sec. 4). Under symmetric conditions the p-PSSW eigenmodes ($p = 0, 1, 2\ldots$) are even (odd) with respect to the layer midplane for even (odd) p. $\delta B_{\text{exc}}(z,t)$ is the optically induced effective field that launches the magnetization precession. It arises from the in-plane rotation of the magnetic easy axis induced by transient thermal effects or by the optical spin-orbit torque [30]. $\delta B_{\text{exc}}(z,t)$ is taken as a product of time and space functions $f(t)g(z)$. $f(t)$ is chosen so that the calculated $\delta\theta(t)$ and $\delta\phi(t)$ match the experimental ones. $g(z)$ is taken as a Fourier series over the PSSW eigenmodes (see Appendix Sec. 4). The depth dependence of the magnetization trajectory for the $p = 0, 1, 2$ SW modes [with time dependence $\cos(2\pi f_p t + \phi_p)$] is shown in Figs. 2(a)–2(c), respectively. It is seen that inside the layer the direction of rotation is the same for the three modes. For

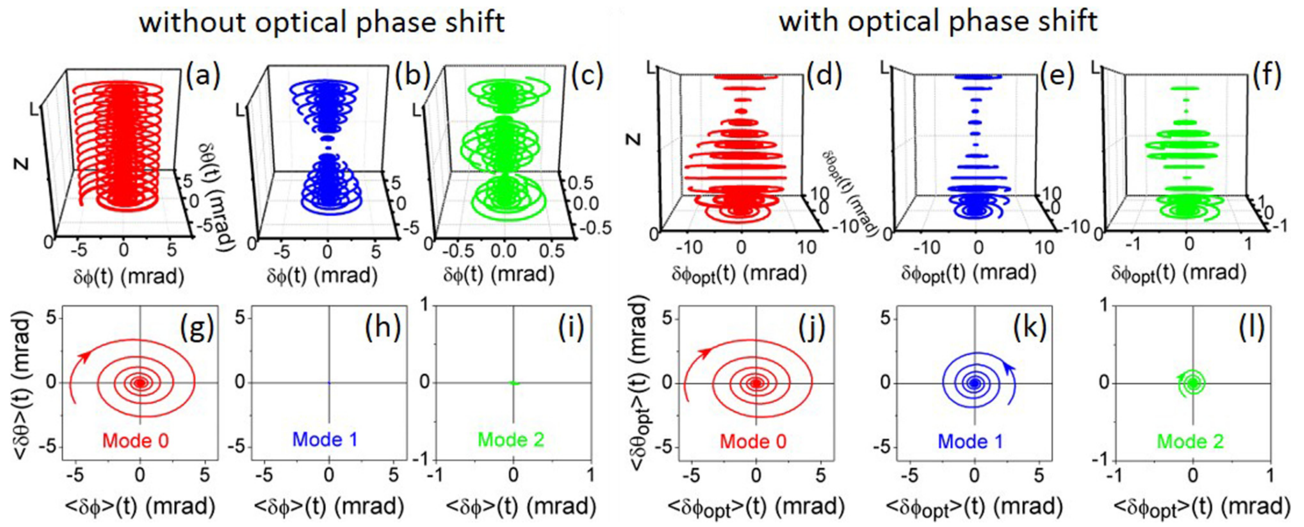

FIG. 2. (left) Magnetization trajectory in the depth of the ferromagnetic layer for the $p = 0$ (a), $p = 1$ (b), $p = 2$ (c) PSSW modes and corresponding detected trajectory in (g), (h), (i) assuming that the optical signal would result from a depth-averaged amplitude. (right) (d), (e), (f) Theoretical effective magnetization trajectory in the depth of the ferromagnetic layer taking into account the optical phase factor and corresponding optically detected trajectory in (j), (k), (l). $L = 50$ nm, $\lambda = 700$ nm, and the other parameters are given in the Appendix.

modes 1 and 2 the magnetization vector experiences a π shift at each node, but its direction of rotation does not change with z [Figs. 2(b) and 2(c)].

The TRMO signal is then calculated using a multilayer and transfer matrix model to obtain the Kerr and Voigt rotation angle and ellipticity. The magnetic layer of thickness L is divided in N sublayers with magnetization components $M(m_{x,y} + \delta m_{x,y,z}(z_i,t))$ (Fig. 4 in the Appendix). The calculation is performed for normal incidence of light along the z direction and linear polarization making an angle β with the x axis. The theoretical dynamical polarization rotation $\delta\beta_r^{\rm th}(t)$ is obtained by taking the limit of an infinite number of sublayers ($N \to \infty$). $\delta\beta_r^{\rm th}(t)$ is the sum of the Kerr and Voigt rotation angles, $\delta\beta_r^{\rm th}(t) = \delta\beta_{K_r}^{\rm th}(t) + \delta\beta_{V_r}^{\rm th}(t)\cos 2(\beta - \phi_0)$ with:

$$\delta\beta_{K_r}^{\rm th}(t) = -\frac{4\pi}{\lambda}\mathrm{Re}\left[\frac{n^2 Q}{n^2-1}\int_0^L e^{i\frac{4\pi n z}{\lambda}}\delta\theta(z,t)dz\right]$$

$$\delta\beta_{V_r}^{\rm th}(t) = \frac{4\pi}{\lambda}\mathrm{Im}\left[\frac{n^2 B}{(n^2-1)}\int_0^L e^{i\frac{4\pi n z}{\lambda}}\delta\phi(z,t)dz\right], \quad (3)$$

where $B = B_1 + Q^2$. Q ($\propto M$) and B_1 ($\propto M^2$) are the elements of the dielectric permittivity tensor describing the Kerr and Voigt effects, respectively (see Appendix Sec. 1). $n = \eta + i\kappa$ is the layer mean complex refractive index and $e^{i\frac{4\pi n z}{\lambda}} = e^{-\alpha z}e^{i\frac{4\pi\eta z}{\lambda}}$ with $\alpha = \frac{4\pi\kappa}{\lambda}$ the absorption coefficient.

V. DISCUSSION

The important result is the modulation of the spatial dependence of the $\delta\theta(z,t)$ and $\delta\phi(z,t)$ magnetization components by the optical phase factor $e^{i\frac{4\pi\eta z}{\lambda}}$ that reflects the propagation of light from the surface to the depth z and back. The phase factor is damped by the $e^{-\alpha z}$ absorption factor. Therefore, in the case of strong absorption as in metallic layers, the TRMO signal will be sensitive only to the SW amplitude very close to the surface within the absorption depth. In the case of weak absorption and layer thickness L comparable to a fraction of the light wavelength inside the material λ/η, the optical phase shift plays a crucial role. It is precisely the case of the sample studied here where $L \approx \lambda/4\eta$.

Actually, for static magnetization, the importance of a phase shift factor that makes the magneto-optical effects sensitive to the magnetization at a specific depth inside single or multiple ferromagnetic layers was theoretically pointed out [31,32] and evidenced experimentally in the 90s [33] and recently in GaMnAs layers [34]. Similar ideas were at play when conceiving magneto-optical sensors using magnetic quantum wells in optical cavities [35] or magnetophotonic crystals with enhanced Faraday rotation [36,37]. However, these ideas had so far not been applied to the time-resolved optical detection of PSSWs in ferromagnetic layers.

The dynamical rotation angles $\delta\beta_{K_r}^{\rm th}(t)$ and $\delta\beta_{V_r}^{\rm th}(t)$ are calculated according to Eq. (3) with the real and imaginary parts of Q and B extracted from the static rotation and ellipticity using Eqs. (A11) and (A19) of the Appendix. In order to compare the optically detected magnetization trajectory and the theoretical one we define $\delta\theta_{\rm opt}(z,t)$ and $\delta\phi_{\rm opt}(z,t)$ so that:

$$\delta\beta_r^{\rm th}(t) = K_r\langle\delta\theta_{\rm opt}\rangle_z(t) + 2V_r\langle\delta\phi_{\rm opt}\rangle_z(t)\cos 2(\beta - \phi_0), \quad (4)$$

where $\langle\cdots\rangle_z = (1/L)\int_0^L \cdots(z)dz$ denotes the average value over the layer thickness, K_r and V_r are given by Eqs. (A11) and (A19) of the Appendix, respectively, and

$$\delta\theta_{\rm opt}(z,t) = -\frac{1}{K_r}\mathrm{Re}\left[\frac{\phi_{\rm opt} n Q}{(n^2-1)}e^{i\frac{4\pi n z}{\lambda}}\right]\delta\theta(z,t), \quad (5)$$

$$\delta\phi_{\rm opt}(z,t) = \frac{1}{2V_r}\mathrm{Im}\left[\frac{\phi_{\rm opt} n B}{(n^2-1)}e^{i\frac{4\pi n z}{\lambda}}\right]\delta\phi(z,t), \quad (6)$$

with $\phi_{\rm opt} = 4\pi nL/\lambda$ the complex optical phase. Figures 2(d)–2(f) show the depth dependence of the $(\delta\phi_{\rm opt},\delta\theta_{\rm opt})$ parametric plot. The effect of the phase factor $e^{i\frac{4\pi n z}{\lambda}}$ is clearly observed when compared to the $(\delta\phi,\delta\theta)$ trajectory shown in Figs. 2(a)–2(c). Despite the difference between Figs. 2(a) and 2(d), for a uniform SW mode the optically detected trajectory is the same as the simple average of the magnetization dynamics over the layer as expected from the expression of $(K_r,\ Vr)$ [Eqs. (A11), (A19)] and the definition of $(\delta\theta_{\mathrm{opt}},\ \delta\phi_{\mathrm{opt}})$. This is indeed verified in Figs. 2(g)–2(j). The quasiuniform mode 0 is detected as rotating clockwise (CW) with time as dictated by the sign of the gyromagnetic factor. An opposite rotation direction can be expected for a nonuniform SW mode if the sign of either $\langle\delta\theta_{\mathrm{opt}}\rangle$ or $\langle\delta\phi_{\mathrm{opt}}\rangle$ is changed with respect to that of $\langle\delta\theta\rangle$ or $\langle\delta\phi\rangle$. This is indeed what is found for the $p = 1$ odd mode, which rotates counterclockwise (CCW) as shown in Fig. 2(k). The $p = 2$ mode rotates CW like the $p = 0$ mode [Fig. 2(l)].

In order to explain why odd modes may exhibit an apparently inverted direction of rotation when detected optically, we take a simplified model and calculate the sign of the amplitude ratio $\delta\theta_{\mathrm{opt}}(t)/\delta\phi_{\mathrm{opt}}(t)$. The damped p-PSSW mode at frequency f_p is expressed as $\delta\theta_p(z,t) = a_p^\theta \exp(-\chi_p t)\cos(2\pi f_p t)\cos(p\pi z/L)$, $\delta\phi_p(z,t) = a_p^\phi \exp(-\chi_p t)\sin(2\pi f_p t)\cos(p\pi z/L)$. Neglecting absorption, the optical precession amplitudes normalized to the excitation amplitudes a_p^θ and a_p^ϕ are:

$$\delta\theta_p^{\mathrm{opt}} = -\frac{4\pi}{K_r}\frac{\eta}{\eta^2-1}\int_0^\ell \mathrm{Re}[Q\ e^{i4\pi u}]\cos(p\pi u/\ell)du$$

$$\delta\phi_p^{\mathrm{opt}} = \frac{4\pi}{2V_r}\frac{\eta}{\eta^2-1}\int_0^\ell \mathrm{Im}[B\ e^{i4\pi u}]\cos(p\pi u/\ell)du\ , \quad (7)$$

where $\ell = L/(\lambda/\eta)$. It is straightforward to show that for even p (even modes) the ratio $r_p = \delta\theta_p^{\mathrm{opt}}/\delta\phi_p^{\mathrm{opt}}$ is positive and equal to 1. For odd modes, r_p can on the contrary be positive or negative depending on the layer thickness and the ratios B_i/B_r and Q_i/Q_r of the imaginary and real parts of B and Q, respectively. It is moreover independent of p and is given by:

$$r_p^{\mathrm{odd}} = -\frac{\left(\frac{B_i}{B_r}C_l + S_l\right)\left(\frac{Q_i}{Q_r}C_l + S_l\right)}{\left(C_l - \frac{B_i}{B_r}S_l\right)\left(C_l - \frac{Q_i}{Q_r}S_l\right)}, \quad (8)$$

with $C_l = \cos(2\pi\ell)$ and $S_l = \sin(2\pi\ell)$. Therefore the possibility to change the sign of only one of the $\delta\theta$ and $\delta\phi$ components ($r_p < 0$) and hence to observe a change of the direction of rotation is achieved exclusively for the *odd* SW modes. This result is not fully conserved when taking into account absorption as can be seen in Fig. 3 where the direction of rotation (CW, CCW) given from the sign of r_p is plotted in (dark/light) grayscale. However, given our parameters, r_1 is always negative for L in the range 26–72 nm encompassing the layer thickness of our sample (50 nm) while r_0 and r_2 are positive. This is an important result of this paper as it provides a tool to identify PSSW modes.

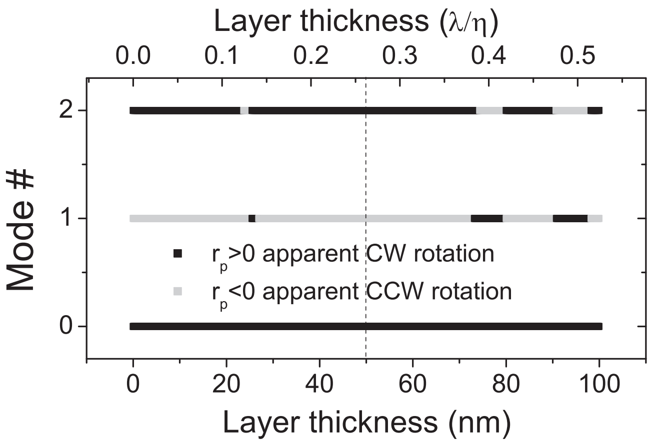

FIG. 3. Theoretical optically detected direction of rotation of the magnetization vector for $p = 0$, 1, and 2 PSSWs modes from the amplitude ratio r_p of $\delta\theta_p^{\mathrm{opt}}$ and $\delta\phi_p^{\mathrm{opt}}$ (see text). The dashed line indicates the layer thickness. $\lambda = 700$ nm, $\eta = 3.67$, $\kappa = 0.1$.

This model also accounts very well for the large amplitude ratio of the high/low frequency modes observed experimentally. If the optically detected signal were proportional to the average of $\delta\theta$ or $\delta\phi$ over the layer thickness [4], $\langle\delta\theta\rangle_z$ and $\langle\delta\phi\rangle_z$, only the uniform PSSW mode should be detected in the case of free boundary conditions, all the higher ones having zero integral. This is illustrated in Figs. 2(h) and 2(i) where the calculated $(\langle\delta\theta\rangle,\langle\delta\theta\rangle)$ signal is zero for the odd $p = 1$ mode and very small for the $p = 2$ mode (it would be strictly zero for zero surface anisotropy). In order to observe higher modes a strong surface pinning would be necessary to give them a nonzero integral. Even then, only the even modes would be detectable since the odd ones would keep a zero integral for symmetric boundary conditions [4]. Our results definitely prove that the high-frequency mode is the first odd mode. This reconciles results obtained by different groups on the determination of the spin stiffness constant that differ by a factor of 4 depending on whether the high-frequency PSSW mode is identified as the $p = 1$ or $p = 2$ mode [8,26]. Furthermore it explains why the TRMO signal can show PSSW modes that are not observed in FMR spectra.

VI. CONCLUSION

In this work we have highlighted the role of the optical phase shift in the amplitude of optically detected SW modes. This solves the mystery of counter-rotating SWs but, more importantly, provides a definite assignment of SW mode number, thereby enabling a reliable determination of the spin stiffness constant with only two optically detected modes. The comprehensive model developed here, which comprises both Kerr and Voigt effects, provides useful guidelines [through Eq. (3)] for optimizing the optical detection of SWs. It may also explain varying SW amplitude ratios observed in different layers/materials [2,26]. It can be straightforwardly extended to longitudinal Kerr and Faraday effects, for which similar effects of the complex optical phase are expected, and therefore be applied to any kind of experimental geometry and magnetic layer, whether ferro-, ferri-, or antiferromagnetic, from metals to insulators.

ACKNOWLEDGMENTS

We thank F. Perez and B. Jusserand for fruitful discussions, B. Eble for cryogenic data, B. Gallas for ellipsometric data, and

M. Bernard, F. Margaillan, F. Breton, S. Majrab, and C. Lelong for technical assistance. This work has been supported by UPMC (Emergence 2012), Region Ile-de-France (DIM Nano-K MURAS2012), and French ANR (ANR13-JS04-0001-01).

APPENDIX

1. Magneto-optical Kerr and Voigt effects

Following Ref. [38], the dielectric tensor for a magnetic cubic crystal is taken as:

$$[\epsilon_{ij}] = \epsilon\left(\begin{bmatrix} 1 & -im_zQ & im_yQ \\ im_zQ & 1 & -im_xQ \\ -im_yQ & im_xQ & 1 \end{bmatrix} + \begin{bmatrix} B_1m_x^2 & B_2m_xm_y & B_2m_xm_z \\ B_2m_xm_y & B_1m_y^2 & B_2m_ym_z \\ B_2m_xm_z & B_2m_ym_z & B_1m_z^2 \end{bmatrix}\right), \tag{A1}$$

with (x,y,z) the standard axes of the cubic lattice, Q the Kerr coefficient (proportional to the saturation magnetization M), and B_1, B_2 the Voigt coefficients (proportional to M^2). Q describes the magnetic circular birefringence and dichroism. (B_1, B_2) describe the magnetic linear birefringence and dichroism. The difference between B_1 and B_2 reflects the deviation from the spherical symmetry. $\mathbf{m} = (m_x, m_y, m_z)$ is the unit magnetization vector. ϵ is the background dielectric constant. The corresponding complex refractive index will be defined as $n^2 = (\eta + i\kappa)^2 = \epsilon$. The sample plane is the (x,y) plane [Fig. 4(a)]. We consider a light beam with normal incidence along the z axis and linear polarization making an angle β with the x axis. The rotation angle $\delta\beta_r$ and ellipticity $\delta\beta_e$ are calculated from the ratio $\chi = b_y/b_x$ of the reflected electric field amplitudes as [39]:

$$\tan 2\delta\beta_r = 2\mathrm{Re}(\chi)/(1-|\chi|^2) \tag{A2}$$

$$\sin 2\delta\beta_e = 2\mathrm{Im}(\chi)/(1+|\chi|^2). \tag{A3}$$

For small rotation and ellipticity the above expressions reduce to:

$$\chi = \tan\beta + (\tan^2\beta + 1)(\delta\beta_r + i\delta\beta_e). \tag{A4}$$

2. Kerr and Voigt rotation and ellipticity for a depth-dependent magnetization

a. Multilayer and transfer matrix model

A multilayer and transfer matrix model is used to calculate the Kerr and Voigt rotation angle and ellipticity in the case of a depth-dependent magnetization. The magnetic layer of total thickness L is divided in N sublayers with thickness $\delta z = L/N$ and magnetization unit vector $\mathbf{m}(z_i)$ (Fig. 4).

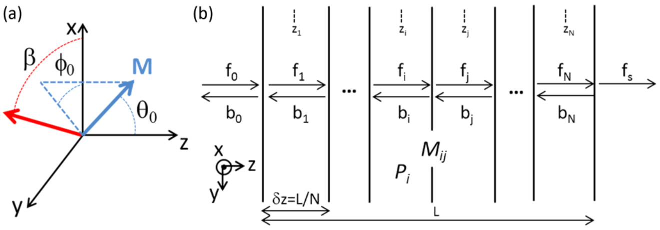

FIG. 4. (a) Reference frame: light propagates along z, **M** is the magnetization vector, β denotes the angle or the linear incident polarization with the x axis. (b) Multilayer scheme.

In the first approach we neglect the Voigt effect ($B_1 = B_2 = 0$). We calculate the Kerr rotation and ellipticity assuming a constant static magnetization in the (x,y) plane and a depth-dependent dynamic magnetization component $m_z(z_i)$ in sublayer i. Because of the low frequency of magnetization precession (GHz) with respect to the light frequency we can regard the problem as a quasistatic one. In each sublayer we consider forward electromagnetic waves propagating as $exp[-i(\omega t - k_i z)]$ with an electric field amplitude $\mathbf{F_i} = (f_{i_x}, f_{i_y})$, an angular frequency ω, and a wave vector $k_i = n_i\omega/c = 2\pi n_i/\lambda$, where λ is the light wavelength. The backward propagating waves are denoted as $\mathbf{B_i}exp[-i(\omega t + k_i z)]$ with $\mathbf{B_i} = (b_{i_x}, b_{i_y})$. The goal of the calculation is to obtain an expression for the reflected amplitudes (b_{0_x}, b_{0_y}) from which the Kerr rotation and ellipticity can then be derived. The propagation equation is solved to obtain the eigenmodes and their corresponding refractive indices. The amplitude of the incoming and reflected waves in layer 0 (vacuum) are related to the amplitude of the outgoing waves into the substrate (layer s) by:

$$\begin{pmatrix} f_{0_x} \\ b_{0_x} \\ f_{0_y} \\ b_{0_y} \end{pmatrix} = \left(\prod_{i=0}^{N-1} M_{i,i+1}P_{\mathrm{i}+1}\right) M_{Ns} \begin{pmatrix} f_{s_x} \\ 0 \\ f_{s_y} \\ 0 \end{pmatrix}. \tag{A5}$$

The transfer matrices M_{ij} relate the amplitudes of the forward and backward propagating waves for the electric field on each side of the interface between layer i and layer j [Fig. 4(b)]:

$$M_{ij} = \frac{1}{t_{ij}} \begin{pmatrix} 1 & r_{\mathrm{ij}} & -i\ Q_{\mathrm{ij}} & i\ Q_{\mathrm{ij}} \\ r_{\mathrm{ij}} & 1 & i\ Q_{\mathrm{ij}} & -i\ Q_{\mathrm{ij}} \\ i\ Q_{\mathrm{ij}} & -i\ Q_{\mathrm{ij}} & 1 & r_{\mathrm{ij}} \\ -i\ Q_{\mathrm{ij}} & i\ Q_{\mathrm{ij}} & r_{\mathrm{ij}} & 1 \end{pmatrix}, \tag{A6}$$

with $Q_{ij} = (m_z(z_i) - m_z(z_j))\,Q\,t_{ji}/4$. The amplitude reflection and transmission coefficients are $r_{ij} = (n_i - n_j)/(n_i + n_j)$ and $t_{ij} = 2n_i/(n_i + n_j)$ with $n_0 = 1$, $n_i = n$ for $i = 1$ to N with $n = \eta + i\kappa$ and $n_{N+1} = n_s$ for the substrate. The amplitudes at the left and right interfaces of layer i are related by the transfer matrix P_i [Fig. 4(b)]:

$$P_i = \begin{pmatrix} e^{-i\phi_i} & 0 & 0 & 0 \\ 0 & e^{i\phi_i} & 0 & 0 \\ 0 & 0 & e^{-i\phi_i} & 0 \\ 0 & 0 & 0 & e^{i\phi_i} \end{pmatrix}, \tag{A7}$$

with $\phi_i = n_i \omega \delta z / c = 2\pi n_i L/(N\lambda)$. From the calculation of the reflected waves the complex quantity $\delta\beta_K = \delta\beta_{K_r} + i\delta\beta_{K_e}$ is obtained. Its expression to the first order in the Kerr coefficient Q and layer-substrate reflexion coefficient $r_{ls} = (n - n_s)/(n - n_s)$ is:

$$\delta\beta_K = \frac{2nQ}{n^2-1}\sin\left(\frac{2\pi nL}{\lambda N}\right)\left(\sum_{i=1}^{N} m_z(z_i) e^{\frac{4i\pi n z_i}{\lambda}}\right) \times \left(1 + \frac{2(n^2+1)e^{i\frac{2\pi nL}{\lambda}} r_{\mathrm{ls}}}{n^2-1}\right). \tag{A8}$$

In the limit $N \to \infty$ it gives:

$$\delta\beta_K = \frac{4\pi}{\lambda}\frac{n^2 Q}{n^2-1}\left(\int_0^L m_z(z) e^{\frac{4i\pi nz}{\lambda}}\, dz\right) \times \left(1 + \frac{2(n^2+1)e^{i\frac{2\pi nL}{\lambda}} r_{\mathrm{ls}}}{n^2-1}\right) \tag{A9}$$

The Kerr rotation angle $\delta\beta_{K_r}$ and ellipticity $\delta\beta_{K_e}$ can then be calculated as $\delta\beta_{K_r} = \mathrm{Re}[\delta\beta_K]$ and $\delta\beta_{K_e} = \mathrm{Im}[\delta\beta_K]$.

In the following, for the sake of simplicity, we will neglect the correction arising from the layer-substrate reflexion coefficient r_{ls}, which for our samples will be negligible ($r_{ls} \approx -8 \times 10^{-3}$). Concerning the m_z dependence of the Kerr signal the result is then the same for a static magnetization aligned along z or a static magnetization in the (x,y) plane with a small dynamical component along z.

b. Static and dynamic Kerr rotation and ellipticity

In the case of spatially uniform magnetization component $m_z = \cos\theta_0$, the static Kerr rotation $\delta\beta^s_{K_r}$ and ellipticity $\delta\beta^s_{K_e}$ are obtained from:

$$\delta\beta^s_{K_r} + i\delta\beta^s_{K_e} = -(K_r + iK_e)\cos\theta_0\ , \text{ with} \tag{A10}$$

$$K_r + i\,K_e = \frac{-i\,nQ}{n^2-1}(1 - e^{i\phi_{\mathrm{opt}}}) \tag{A11}$$

$$= \frac{-i\,nQ}{n^2-1}(1 - e^{-\alpha L} e^{i\varphi_{\mathrm{opt}}}), \tag{A12}$$

with $\phi_{\mathrm{opt}} = 4\pi nL/\lambda$ the complex optical phase, $\varphi_{\mathrm{opt}} = 4\pi\eta L/\lambda$, and $\alpha = 4\pi\kappa/\lambda$ the absorption coefficient. These expressions can also be obtained from a standard two-layer interference model [34,35]. For strong absorption ($\alpha L \gg 1$), typically in thin metallic layers, or more generally for a magnetic layer much thicker than the absorption length, the Kerr coefficients K_r and K_e for rotation and ellipticity, respectively, take the form calculated for a semi-infinite magnetic medium [39]: $K^\infty_r = \mathrm{Im}[\frac{nQ}{n^2-1}]$ and $K^\infty_e = -\mathrm{Re}[\frac{nQ}{n^2-1}]$. For a thick layer ($L \gg \alpha^{-1}$) but in the case of weak absorption ($\kappa \ll \eta$), these Kerr coefficients can be written as:

$$K^\infty_r = \frac{(\eta^2-1)\eta\, Q_i - (\eta^2+1)\kappa\, Q_r}{(\eta^2-1)^2}$$

$$K^\infty_e = -\frac{(\eta^2-1)\eta\, Q_r + (\eta^2+1)\kappa\, Q_i}{(\eta^2-1)^2}, \tag{A13}$$

with Q_r (Q_i), the real (imaginary) part of Q.

For weak absorption, typically in semiconductors, and/or for a thin layer with respect to the absorption length, the Kerr coefficients are modulated by the optical phase factor φ_{opt} and therefore depend on the layer thickness. Taking $\kappa \ll \eta$, one obtains:

$$K_r = K^\infty_r + \exp(-\alpha L)(-K^\infty_r \cos\varphi_{\mathrm{opt}} + K^\infty_e \sin\varphi_{\mathrm{opt}})$$

$$K_e = K^\infty_e - \exp(-\alpha L)(K^\infty_e \cos\varphi_{\mathrm{opt}} + K^\infty_r \sin\varphi_{\mathrm{opt}}). \tag{A14}$$

We see that the Kerr rotation and ellipticity coefficients of a layer with finite thickness are expressed as a linear combination of those for the infinitely thick layer. From the experimental static Kerr rotation and ellipticity, the real and imaginary parts of Q can be obtained using Eqs. (A13) and (A14) provided the complex refractive index is known.

In the case of a static equilibrium magnetization in the (x,y) plane ($\theta_0 = \pi/2$) and small time- and depth-dependent magnetization along z (perpendicular standing spin waves for instance) then $m_z = -\delta\theta$ and the dynamic Kerr rotation and ellipticity are written:

$$\delta\beta_{K_r}(t) + i\ \delta\beta_{K_e}(t) = -\frac{4\pi}{\lambda}\frac{n^2 Q}{n^2-1}\int_0^L e^{i\frac{4\pi nz}{\lambda}}\,\delta\theta(z,t)dz. \tag{A15}$$

In the case of a z-independent (flat) profile $\delta\beta_{K_r}(t)$ and $\delta\beta_{K_e}(t)$ are simply expressed as: $\delta\beta_{K_r}(t) = K_r\delta\theta(t)$ and $\delta\beta_{K_e}(t) = K_e\delta\theta(t)$. In order to compare the dynamics of spin waves with z-independent and z-dependent profiles we define an apparent (optical) $\delta\theta$ whose average over the layer thickness L is:

$$\langle\delta\theta_{\mathrm{opt}}\rangle_z(t) = -\frac{1}{K_r}\frac{4\pi L}{\lambda}\mathrm{Re}\left[\frac{n^2 Q}{n^2-1}\frac{1}{L}\int_0^L e^{i\frac{4\pi nz}{\lambda}}\,\delta\theta(z,t)dz\right]. \tag{A16}$$

c. Static and dynamic Voigt rotation and ellipticity

The magnetic linear birefringence and dichroism (Voigt effect) can be calculated along the same lines. The static Voigt rotation and ellipticity for a depth-independent magnetization are:

$$\delta\beta^s_{V_r} + i\ \delta\beta^s_{V_e} = -\frac{n}{2(n^2-1)}[(B_1 + Q^2)\sin 2\beta\cos 2\phi_0 - (B_2 + Q^2)\cos 2\beta\sin 2\phi_0]\sin^2\theta_0(1 - e^{i\phi_{\mathrm{opt}}}). \tag{A17}$$

In the following we will neglect the small deviation from the spherical approximation arising from the cubic symmetry and take $B_2 = B_1$. We then have

$$\delta\beta^s_{V_r} + i\ \delta\beta^s_{V_e} = -(V_r + i\ V_e)\sin^2\theta_0 \sin 2(\beta - \phi_0) \text{ with} \tag{A18}$$

$$V_r + i\ V_e = \frac{nB}{2(n^2-1)}(1 - e^{i\phi_{\mathrm{opt}}}), \tag{A19}$$

where we have defined as V_r and V_e the Voigt coefficients related to rotation and ellipticity, respectively, and we have set $B = B_1 + Q^2$. For an in-plane spatially uniform static equilibrium magnetization and a small $\delta\phi(z,t)$ component the

Voigt rotation and ellipticity are expressed as:

$$\delta\beta_{V_r}(t) + i\ \delta\beta_{V_e}(t) = \left(-\frac{i\ 4\pi}{\lambda}\frac{n^2B}{(n^2-1)}\int_0^L e^{i\frac{4\pi nz}{\lambda}}\delta\phi(z,t)dz\right) \times \cos 2(\beta-\phi_0). \tag{A20}$$

Given that in the case of a z-independent spin wave amplitude $\delta\beta_{V_r}(t)$ is simply expressed as $\delta\beta_{V_r}(t) = 2V_r\delta\phi(t)\cos 2(\beta - \phi_0)$, we also define an optical $\delta\phi$ by

$$\langle\delta\phi_{\text{opt}}\rangle_z(t) = \frac{1}{2V_r}\frac{4\pi L}{\lambda}\text{Im}\left[\frac{n^2B}{(n^2-1)}\frac{1}{L}\int_0^L e^{i\frac{4\pi nx}{\lambda}}\delta\phi(z,t)dz\right]. \tag{A21}$$

d. Total static and dynamic polarization rotation

To summarize, taking into account the Kerr and Voigt effects the static polarization rotation is expressed as:

$$\begin{aligned}\delta\beta_r^s &= \delta\beta_{K_r}^s + \delta\beta_{V_r}^s\\ &= -K_r\cos\theta_0 - V_r\sin^2\theta_0\sin 2(\beta-\phi_0)\ .\end{aligned} \tag{A22}$$

For in-plane static magnetization ($\theta_0 = \pi/2$) the dynamic polarization rotation is the sum of the Kerr and Voigt contributions and reads:

$$\begin{aligned}\delta\beta_r(t) &= \delta\beta_{K_r}^{\text{th}}(t) + \delta\beta_{V_r}^{\text{th}}(t)\cos 2(\beta-\phi_0)\\ &= \frac{4\pi}{\lambda}\left(\text{Re}\left[\frac{-n^2Q}{n^2-1}\int_0^L e^{i\frac{4\pi nz}{\lambda}}\delta\theta(z,t)dz\right]\right.\\ &\quad\left.+\,\text{Im}\left[\frac{n^2B}{2(n^2-1)}\int_0^L e^{i\frac{4\pi nz}{\lambda}}\delta\phi(z,t)dz\right]\cos 2(\beta-\phi_0)\right)\\ &= K_r\langle\delta\theta_{\text{opt}}\rangle_z(t) + 2V_r\langle\delta\phi_{\text{opt}}\rangle_z(t)\cos 2(\beta-\phi_0).\end{aligned} \tag{A23}$$

3. Magnetization precession from the magneto-optical signal

The experimental dynamic magneto-optical signal $\delta\beta_r^{\text{exp}}(t)$ contains $\delta\theta^{\text{exp}}(t)$ and $\delta\phi^{\text{exp}}(t)$ contributions but also a nonoscillating $\delta M(t)$ contribution from the dependence of K_r and V_r on the modulus M of the magnetization ($Q \propto M$ and $B \propto M^2$) [9]. The $\delta\phi^{exp}(t)$ and $\delta M(t)$ contributions both depend on the angle between the linear polarization and the magnetization $(\beta - \phi_0)$. We then have:

$$\begin{aligned}\delta\beta_r^{\text{exp}}(t,\beta) &= K_r\delta\theta^{\text{exp}}(t) + 2V_r\delta\phi^{\text{exp}}(t)\cos 2(\beta-\phi_0)\\ &\quad -2V_r\frac{\delta M(t)}{M}\sin 2(\beta-\phi_0)\ .\end{aligned} \tag{A24}$$

The experimental signal $\delta\beta_r^{\text{exp}}(t,\beta)$ is then fitted by a combination of polarization-dependent and independent terms: $u(t) + v(t)\sin 2\beta + w(t)\cos 2\beta$. One then has $\delta\theta^{\text{exp}}(t) = u(t)$, $\delta\phi^{\text{exp}}(t) = [w(t)\cos 2\phi_0 + v(t)\sin 2\phi_0]/2V_r$, $\delta M(t)/M = [w(t)\sin 2\phi_0 - v(t)\cos 2\phi_0]/2V_r$. The ϕ_0 angle that provides a nonoscillating $\delta M(t)/M$ signal ($\phi_0 \approx 0$) is in good agreement with the one calculated from the minimization of the magnetic energy ($\phi_0 = 5^\circ$) (see below).

4. Optical excitation of spin waves

The magnetization precession is calculated by solving the small-angle approximation of the Landau-Lifschitz-Gilbert (LLG) equation for in-plane static magnetization.

$$\begin{aligned}\delta\dot{\phi} &= \gamma\left(F_{\theta\theta}\ \delta\theta + F_{\theta\phi}\ \delta\phi - D\frac{\partial^2\delta\theta}{\partial z^2}\right) + \alpha_G\delta\dot{\theta}\\ \delta\dot{\theta} &= -\gamma\left(F_{\phi\theta}\ \delta\theta + F_{\phi\phi}\ \delta\phi - D\frac{\partial^2\delta\phi}{\partial z^2} + \delta B_{\text{exc}}(z,t)\right) - \alpha_G\ \delta\dot{\phi},\end{aligned} \tag{A25}$$

with $\delta\theta$ and $\delta\phi$ the time-dependent parts of the polar and azimuthal angles of the magnetization vector $\mathbf{M}$, respectively (Fig. 4). F is equal to E/M where E is the magnetic anisotropy energy taken as [29]

$$\begin{aligned}E &= \left(\frac{\mu_0M^2}{2} - K_{2\perp}\right)\cos^2\theta - K_{2\parallel}\sin^2\theta\sin^2\left(\frac{\pi}{4}-\phi\right)\\ &\quad -\frac{K_{4\parallel}}{8}\sin^4\theta(3+\cos 4\phi) - \frac{K_{4\perp}}{2}\cos^4\theta,\end{aligned} \tag{A26}$$

where $K_{2\perp}$, $K_{2\parallel}$ are the uniaxial out-of-plane and in-plane anisotropy constants, respectively, and $K_{4\perp}$, $K_{4\parallel}$ describe the biaxial anisotropy. $F_{i,j} = \frac{\partial^2 F}{\partial i\partial j}$ are the second derivatives of F with respect to the angles (i,j). α_G is the Gilbert damping parameter. $D = 2A/M$ is the spin stiffness constant with A the exchange constant. $\delta B_{\text{exc}}(z,t)$ is the optically induced effective field that launches the magnetization precession. It arises from the transient in-plane change of the magnetic easy axis [30]. $\delta B_{\text{exc}}(z,t)$ is chosen as a product of time and space functions. The transient time behavior of δB_{exc} is chosen as a normalized sum of rising and decaying exponentials with time constants 0.03 ns and 1 ns, respectively, so as to give the best match to the experimental dynamical Kerr and Voigt signals and to be consistent with the time behavior of $\delta M(t)$. The spatial profile of $\delta B_{\text{exc}}(z,t)$ is taken as a Fourier series over the eigenmodes of the perpendicular standing spin waves with amplitude $a_p\delta B_{\text{exc}}^0/p!$ for mode p. Equation (A25) is solved using Rado-Weertman boundary conditions [8,40] with a very small surface anisotropy energy $K_s = -1\,\mu\text{J}\,\text{m}^{-2}$ so as to match the mode 0 experimental frequency with the one calculated using the magnetic anisotropy constants. These anisotropy constants and the magnetization used in the calculation are determined by ferromagnetic resonance and superconducting quantum interference device experiments, respectively. At the working temperature $T = 12$ K, the anisotropy constants are $K_{2\perp} = -239\,\text{J}\,\text{m}^{-3}$, $K_{2\parallel} = 214\,\text{J}\,\text{m}^{-3}$, $K_{4\perp} = 977\,\text{J}\,\text{m}^{-3}$, $K_{4\parallel} = 1210\,\text{J}\,\text{m}^{-3}$, the magnetization is $M = 38.4\,\text{kA}\,\text{m}^{-1}$, the g factor is $g = 1.92$ [41]. We take $\eta = 3.67$ [42], $\kappa = 0.1$, $K_r = -7$ mrad, $K_e = 7$ mrad, $V_r = -0.7$ mrad, $V_e = 0.6$ mrad. The best fit with experimental results is obtained for values of the parameters $A = 0.28\,\text{pJm}^{-1}$, $\delta B_{\text{exc}}^0 = -0.34\,\text{mT}$, $a_0 = 1$, $|a_p| = 1.58$ for $p > 0$.

[1] E. Beaurepaire, J.-C. Merle, A. Daunois, and J. Bigot, Phys. Rev. Lett. **76**, 4250 (1996).
[2] M. van Kampen, C. Jozsa, J. Kohlhepp, P. LeClair, L. Lagae, W. de Jonge, and B. Koopmans, Phys. Rev. Lett. **88**, 227201 (2002).
[3] J. Kisielewski, A. Kirilyuk, A. Stupakiewicz, A. Maziewski, A. Kimel, T. Rasing, L. T. Baczewski, and A. Wawro, Phys. Rev. B **85**, 184429 (2012).
[4] D. M. Wang, Y. H. Ren, X. Liu, J. K. Furdyna, M. Grimsditch, and R. Merlin, Phys. Rev. B **75**, 233308 (2007).
[5] Y. Hashimoto, S. Kobayashi, and H. Munekata, Phys. Rev. Lett. **100**, 067202 (2008).
[6] J. Qi, Y. Xu, A. Steigerwald, X. Liu, J. K. Furdyna, I. E. Perakis, and N. H. Tolk, Phys. Rev. B **79**, 085304 (2009).
[7] E. Rozkotova, P. Nemec, P. Horodyska, D. Sprinzl, F. Trojanek, P. Maly, V. Novak, K. Olejnik, M. Cukr, and T. Jungwirth, Appl. Phys. Lett. **92**, 122507 (2008).
[8] S. Shihab, H. Riahi, L. Thevenard, H. J. von Bardeleben, A. Lemaître, and C. Gourdon, Appl. Phys. Lett. **106**, 142408 (2015).
[9] P. Němec, V. Novák, N. Tesařová, E. Rozkotová, H. Reichlová, D. Butkovičová, F. Trojánek, K. Olejník, P. Malý, R. P. Campion, B. L. Gallagher, J. Sinova, and T. Jungwirth, Nat. Commun. **4**, 1422 (2013).
[10] F. Hansteen, A. Kimel, A. Kirilyuk, and T. Rasing, Phys. Rev. Lett. **95**, 047402 (2005).
[11] A. Kirilyuk, A. V. Kimel, and T. Rasing, Rep. Prog. Phys. **76**, 026501 (2013).
[12] S. Mangin, M. Gottwald, C.-H. Lambert, D. Steil, V. Uhlí, L. Pang, M. Hehn, S. Alebrand, M. Cinchetti, G. Malinowski, Y. Fainman, M. Aeschlimann, and E. E. Fullerton, Nat. Mater. **13**, 286 (2014).
[13] Y. Kajiwara, K. Harii, S. Takahashi, J. Ohe, K. Uchida, M. Mizuguchi, H. Umezawa, H. Kawai, K. Ando, K. Takanashi, S. Maekawa, and E. Saitoh, Nature (London) **464**, 262 (2010).
[14] B. Lenk, H. Ulrichs, F. Garbs, and M. Münzenberg, Phys. Rep. **507**, 107 (2011).
[15] S. O. Demokritov, B. Hillebrands, and A. N. Slavin, Phys. Rep. **348**, 441 (2001).
[16] E. Rozkotova, P. Nemec, N. Tesarova, P. Maly, V. Novak, K. Olejnik, M. Cukr, and T. Jungwirth, Appl. Phys. Lett. **93**, 232505 (2008).
[17] Y. Hashimoto and H. Munekata, Appl. Phys. Lett. **93**, 202506 (2008).
[18] F. Teppe, M. Vladimirova, D. Scalbert, M. Nawrocki, and J. Cibert, Solid State Commun. **128**, 403 (2003).
[19] N. Tesařová, P. Nêmec, E. Rozkotová, J. Šubrt, H. Reichlová, D. Butkoviĉová, F. Trojánek, P. Malý, V. Novák, and T. Jungwirth, Appl. Phys. Lett. **100**, 102403 (2012).
[20] A. M. Kalashnikova, A. V. Kimel, R. V. Pisarev, V. N. Gridnev, P. A. Usachev, A. Kirilyuk, and Th. Rasing, Phys. Rev. B **78**, 104301 (2008).
[21] Z. Liu, F. Giesen, X. Zhu, R. D. Sydora, and M. R. Freeman, Phys. Rev. Lett. **98**, 087201 (2007).
[22] M. Bombeck, A. S. Salasyuk, B. A. Glavin, A. V. Scherbakov, C. Brüggemann, D. R. Yakovlev, V. F. Sapega, X. Liu, J. K. Furdyna, A. V. Akimov, and M. Bayer, Phys. Rev. B **85**, 195324 (2012).
[23] J. Hamrle, J. Pištora, B. Hillebrands, B. Lenk, and M. Münzenberg, J. Phys. D: Appl. Phys. **43**, 325004 (2010).
[24] C. Kittel, Phys. Rev. **110**, 1295 (1958).
[25] J. Wu, N. D. Hughes, J. R. Moore, and R. J. Hicken, J. Magn. Magn. Mater. **241**, 96 (2002).
[26] N. Tesařová, D. Butkovičová, R. P. Campion, A. W. Rushforth, K. W. Edmonds, P. Wadley, B. L. Gallagher, E. Schmoranzerová, F. Trojánek, P. Malý, P. Motloch, V. Novák, T. Jungwirth, and P. Němec, Phys. Rev. B **90**, 155203 (2014).
[27] S. Shihab, L. Thevenard, A. Lemaître, J.-Y. Duquesne, and C. Gourdon, J. Appl. Phys. **119**, 153904 (2016).
[28] A. V. Kimel, G. V. Astakhov, A. Kirilyuk, G. M. Schott, G. Karczewski, W. Ossau, G. Schmidt, L. W. Molenkamp, and T. Rasing, Phys. Rev. Lett. **94**, 227203 (2005).
[29] M. Cubukcu, H. J. von Bardeleben, J. L. Cantin, and A. Lemaître, Appl. Phys. Lett. **96**, 102502 (2010).
[30] N. Tesařová, P. Němec, E. Rozkotová, J. Zemen, T. Janda, D. Butkovičová, F. Trojánek, K. Olejník, V. Novák, P. Malý, and T. Jungwirth, Nat. Phot. **7**, 492 (2013).
[31] G. Traeger, L. Wenzel, and A. Hubert, Phys. Status Solidi A **131**, 201 (1992).
[32] A. Hubert and G. Traeger, J. Magn. Magn. Mater. **124**, 185 (1993).
[33] G. Pénissard, P. Meyer, J. Ferré, and D. Renard, J. Magn. Magn. Mater. **146**, 55 (1995).
[34] H. Terada, S. Ohya, and M. Tanaka, Appl. Phys. Lett. **106**, 222406 (2015).
[35] C. Gourdon, V. Jeudy, M. Menant, D. Roditchev, L. A. Tu, E. L. Ivchenko, and G. Karczewski, Appl. Phys. Lett. **82**, 230 (2003).
[36] M. Inoue, K. Arai, T. Fujii, and M. Abe, J. Appl. Phys. **83**, 6768 (1998).
[37] I. L. Lyubchanskii, N. N. Dadoenkova, M. I. Lyubchanskii, E. A. Shapovalov, and T. Rasing, J. Phys. D: Appl. Phys. **36**, R277 (2003).
[38] A. Hubert, R. Schäfer, *Magnetic Domains* (Springer, Berlin, Heidelberg, New York, 2009).
[39] A. K. Zvezdin and V. A. Kotov, *Modern Magnetooptics and Magnetooptical Materials* (CRC Press, New York, 1997).
[40] G. T. Rado and J. R. Weertman, J. Phys. Chem. Solids **11**, 315 (1959).
[41] M. Cubukcu, H. J. von Bardeleben, K. Khazen, J. L. Cantin, O. Mauguin, L. Largeau, and A. Lemaître, Phys. Rev. B **81**, 041202 (2010).
[42] B. Gallas (private communication).